Chinese Journal of
POLYMER SCIENCE

RESEARCH ARTICLE

https://doi.org/10.1007/s10118-024-3144-2
Chinese J. Polym. Sci. **2024**, *42*, 992–1001

An Effective Approach for the Preparation of High Performance Thermal Conductive Polymer Composites Containing Liquid Metal

Xin Chen[a], Xue-Zhong Zhang[a], Yi-Fei Yuan[b], Chuan-Liang Chen[a], Lian-Hu Xiong[a], Qiang Fu[a], and Hua Deng[a*]

[a] *College of Polymer Science and Engineering, State Key Laboratory of Polymer Materials Engineering, Sichuan University, Chengdu 610065, China*
[b] *Department of Materials Science and Engineering, Sichuan University-Pittsburgh Institute, Sichuan University, Chengdu 610065, China*

Electronic Supplementary Information

Abstract The preparation of high-performance thermal conductive composites containing liquid metals (LM) has attracted significant attention. However, the stable dispersion of LM within polymer solution and effective property contribution of liquid metals remains significant challenges that need to be overcome. Inspired by the properties of the dendritic structure of the tree root system in grasping the soil, "shear-induced precipitation-interfacial reset-reprotonation" processing strategy is proposed to prepare nanocomposites based on aramid micron fibers (AMFs) with hierarchical dendritic structure. Thanks to the combination of van der Waals force provided by hierarchical dendritic structure, electrostatic interaction between AMFs and LM, coordinative bonding of —NH to LM, together with interfacial re-setting and multi-step protonation, several features can be achieved through such strategy: conducive to the local filler network construction, improvement of interfacial interaction, improvement of the stability of filler dispersion in the solvent, and enhancement of mechanical and thermal properties of the films. The resulting AMFs-pH=4/LM films demonstrate a thermal conductivity of 10.98 $W \cdot m^{-1} \cdot K^{-1}$ at 70% filler content, improvement of 126.8% compared to ANFs/LM film; while maintaining a strength of ~85.88 MPa, improvement of 77% compared to AMFs/LM film. They also possess insulation properties, enable heat dissipation for high power electronics. This work provides an effective strategy for the preparation of high performance polymer composites containing liquid metal.

Keywords Shear-induced; Reprotonation; AMFs; LM; Filler dispersion

Citation: Chen, X.; Zhang, X. Z.; Yuan, Y. F.; Chen, C. L.; Xiong, L. H.; Fu, Q.; Deng, H. An effective approach for the preparation of high performance thermal conductive polymer composites containing liquid metal. *Chinese J. Polym. Sci.* **2024**, *42*, 992–1001.

INTRODUCTION

Effective heat dissipation is of paramount importance in the field of electronics.[1–7] Thermal conductivity plays a crucial role in the domain of heat dissipation. Materials with high thermal conductivity efficiently transfer and dissipate generated heat, thereby upholding optimal operating temperature of the equipment. By enhancement of material thermal conductivity, the temperature of the equipment can be effectively mitigated, thereby ameliorating its performance, reliability, and longevity.[8–10]

Polymers are generally poor conductors of heat,[11,12] so it is necessary to introduce highly thermal conductive fillers to prepare composites to achieve high thermal conductivity. Typically, liquid metal, as a unique thermally conductive filler, possesses the advantageous combination of room temperature deformability inherent to liquids and the high thermal conductivity characteristic of metals.[13–16] As a result, it can effectively serve as a thermal bridge, reducing the contact thermal resistance between the adjacent matrix and filler. Notably, gallium-based liquid metal (LM) with its exceptionally high intrinsic thermal conductivity (39 $W \cdot m^{-1} \cdot K^{-1}$) has garnered significant attention in the realm of flexible polymer-based multifunctional composites.[17] In this study, the term "liquid metal" (LM) specifically refers to gallium-based liquid metal. However, during the processing stage, attaining stable and well-dispersed liquid metals in liquid metal-polymer solutions presents a significant challenge due to the pronounced interfacial incompatibility between liquid metals and polymers.[18,19] Successful dispersion of LM within the polymer solution has been achieved through techniques such as "tailored core-shell" structures, surface modification, dispersion of LM into numerous small particles, and rapid matrix curing, for example, Matyjaszewski *et al*. employed atom transfer radical polymerization. Firstly, they utilized a radical polymerization initiator to modify the surface of the liquid metal. After the formation of the core-shell structure, they controlled the preparation conditions to initiate radical polymerization. This process enhances the interaction between the liquid metal and the polymer matrix; Li *et al*. employed ultrasonically triggered *in situ* polymerization of the LM, in a fluid lactone. This

* Corresponding author, E-mail: huadeng@scu.edu.cn
Special Issue: Functional Polymer Materials
Received February 27, 2024; Accepted April 12, 2024; Published online May 21, 2024

process resulted in the formation of a poly(lactone) wrapping, creating a core-shell structure for the LM and facilitating its dispersion within the polymer matrix; Zhang *et al*. enhanced the interaction between PVA and LM by utilizing the self-contained hydrogen bonding between —OH groups on PVA and LM. This interaction effectively stabilizes the LM; Ye *et al*. employed chemical cross-linking between the LM and sulfhydryl groups to enhance the formation of the polymer matrix network.[20–24] However, the utilization of tailored "core-shell" structures or filler surface modifications often results in the encapsulation of the functional filler surface, impeding the localized lapping of the functional filler network.[25] This impediment hampers the effective contribution of functional fillers in composites. To address this challenge effectively, an optimal approach is utilizing fillers for polymer encapsulation and combined with multiple interaction forces to enhance interfacial forces.

It is worth mentioning that, in pursuit of fabricating composites with exceptional performance, the incorporation of aramid nanofibers (ANFs) as the polymer matrix is adopted, owing to the establishment of hydrogen bonding and π-π interactions among ANFs.[26,27] The integration of LM into the ANFs network not only furnishes additional channels for efficient heat dissipation but also capitalizes on the presence of —NH functional groups along the molecular chain of ANFs to facilitate the dispersion of LM. This synergistic interplay between ANFs and LM culminates in the fabrication of films endowed with outstanding properties and performance attributes.[28–31]

Trees, as the most prevalent botanical organisms in nature, consist of dendrites (trunks, branches, roots, *etc*.) that possess several distinctive characteristics. Firstly, these dendrites deeply penetrate the ground, establishing a secure anchorage within the soil. Secondly, the soil envelops and surrounds the dendrites, simultaneously being exposed to external elements. Additionally, the interaction between the soil and tree roots is further enhanced through wetting and subsequent drying processes. Herein, inspired by the properties of the dendritic structure of the tree root system in grasping the soil, we propose an effective processing strategy called "shear-induced precipitation-interfacial reset-reprotonation", provides a promising approach to improve the stable dispersion of LM in the polymer solution. By harnessing van der Waals forces, electrostatic interactions, and coordinative bonding of —NH to LM, the synergy of these forces, coupled with interfacial resetting, enhances the interfacial forces between the LM matrix and the filler, achieve the enhancement of the mechanical and thermal conductivity of composites. The strategy consists of a series of steps to create unique composite material. Firstly, three-dimensional hierarchical structured AMFs, referred to as "tree roots", were prepared through shear-induced precipitation. These hierarchical structured AMFs, provide van der Waals force,[32] featuring —NH functional groups on the molecular chain, facilitate the dispersion of LM. During this process, the AMFs experienced partial protonation. Subsequently, the protonated AMFs were pulverized into zero-dimensional LM particles. Spherical LM particles with a positive charge are then dispersed onto the surface of negatively charged AMFs, resulting in a distinctive "core-shell" structure where the filler coats the polymer. Secondly, the films obtained by vacuum-assisted infiltration (VAF) were subsequently subjected to an isopropanol environment in different pH values, through this process, wetting and drying of "soil" were realized, LM interfacial reset is achieved, leading to improved interactions between the filler and the polymer matrix. Finally, the AMFs undergo reprotonation by immersion in water. The reprotonation process ensures complete protonation of the AMFs, minimizing defects within the film. The resulting AMFs-pH/LM composite exhibits a uniform distribution of LM droplets in the interconnected AMFs network, forming a three-dimensional structure. This unique composite structure gives the film extraordinary properties. At a 70% filler content of pH=4 (0.0001 mol/L HCl), the in-plane thermal conductivity of the film reaches 10.98 $W{\cdot}m^{-1}{\cdot}K^{-1}$, while the film maintains its high strength of approximately 85.88 MPa and insulating properties of 3.07×10^{12} Ω·cm.

EXPERIMENTAL

Materials

The raw PPTA yarns (K49) used in the experiment were purchased from Dupont. Dimethyl sulfoxide (DMSO, AR, ≥99.5%), isopropyl alcohol (IPA, AR, ≥99.5%), and KOH were obtained from Chengdu Kelong Chemical Co., Ltd., China, LM (EGaIn, 75% Ga and 25% In by weight) was procured from Suzhou Star Ocean Business Co. Hydrochloric acid (HCl, 37 wt%) was obtained from Sinopharm Chemical Reagent Co., Ltd. (Shanghai, China). The materials were utilized without undergoing any supplementary purification procedures.

Fabrication of AMFs-pH/LM Films

Fabrication of ANFs and AMFs

In accordance with a prior research,[33] 8 g of Kevlar 49 fibers and 8 g of KOH were initially added to 392 g of DMSO. After 7 days of mechanical agitation at room temperature, a dark red dispersion of ANFs was obtained. The KOH was separated from the solution through centrifugation at 5000 r/min for 10 min, and the resulting solution was further diluted to a 1% weight concentration using DMSO for subsequent use. Subsequently, as depicted in Fig. S1 in the electronic supplementary information (ESI), 1% ANFs/DMSO solution (5 g) was uniformly injected into a high-speed shear IPA turbulent shear field (100 mL) over a duration of 1 min for each time. During this process, DMSO underwent solvent exchange with IPA, while ANFs experienced shear forces within the shear field, resulting in the formation of AMFs. Non-solvent was continuously circulated through an external pipeline. After 5 min of stirring, a dendritic colloidal suspension of AMFs with a solid content of 0.5 mg/mL was obtained. The obtained aramid dendritic particles exhibited colloidal-size characteristics, as confirmed by the presence of the Tyndall effect in the solution. Viscosity tests were conducted on 0.5 mg/mL AMFs/IPA solutions obtained through the utilization of turbulent shear-induced precipitation, as depicted in Fig. S2 (in ESI). The results confirmed that the solutions exhibited turbulent behavior during the shear process.

Fabrication of LM particles and AMFs/LM suspension

LM was dispersed in isopropanol and subjected to sonication for various durations to achieve different sizes of LM particles (Fig.

S9 in ESI). Specifically, we chose a shorter time period appropriate LM sonicated at 600 W for 30 min. The average particle size of LM is 1682 nm. Subsequently, they were mixed with the obtained AMFs dispersion solution under mechanical stirring to form homogeneous AMFs/LM solutions with different mass ratios.

Fabrication of AMFs-pH/LM films

The AMFs/LM suspension were then utilized to prepare AMFs-pH/LM films using the layer-by-layer VAF method. The prepared AMFs were subsequently immersed in solutions with varying pH values for a duration of 2 h. Following a triple rinse with deionized water, they were immersed in a water bath for 24 h to undergo reprotonation. Finally, the films were cold pressed at 25 MPa. For comparison, AMFs/LM and ANFs/LM were prepared by the similar method described above without being immersed in solutions with varying pH and reprotonation.

Characterization

The morphology of AMFs, AMFs/LM particles, AMFs-pH/LM, AMFs/LM films was observed using a polarized light microscope (OM, BX51, Osbalin) and field emission scanning electron microscope (FESEM, Apero S HiVac, FEI, USA), electron microscope (TEM, Tecnai G2 F20 S-TWIN) and atomic force microscope (AFM, Bruker, USA). The zeta potential of AMFs and LM was determined using the Brookhaven Zeta PALS 190 Plus instrument. X-ray photoelectron spectroscopy (XPS) spectra were acquired using a monochromatic Al-Kα X-ray source on an ESCALab Xi^+ instrument (ThermoScientific, USA). The AMFs-pH/LM films were characterized by Fourier-transform infrared spectroscopy (FTIR Nicolet 6700 instrument ThermoScientific USA). The determination of both in-plane and out-of-plane thermal conductivity was accomplished using the equation $k = \alpha \times \rho \times C_p$, where α represents the thermal diffusivity, ρ denotes the density, and C_p signifies the specific heat capacity. The thermal diffusivity (α) measurement was performed using Laser Flash Analysis (LFA 467 Hyper Flash, Netzsch, Germany). The voltage and pulse width parameters were set at 250 V and 200 μs, respectively, for the configuration. The tensile stress-strain curves were obtained by conducting tests on a universal testing instrument (Instron 5967, USA) equipped with a 500 N load cell, the tests were performed at room temperature and under a relative humidity of approximately 50%. The volume resistivity of the films was assessed using an ultra-high resistance micro-current tester (ZST-121, Zhonghang Times Instrument Co., Ltd., China). *In situ* infrared spectra were obtained by ReactIR 701L, liquid nitrogen detector.

RESULTS AND DISCUSSION

Fig. 1(a) presents a schematic diagram illustrating the preparation process of AMFs/LM nanocomposite membranes through "shear-induced precipitation-interfacial reset-reprotonation" then vacuum-assisted filtration. Following the shear-induced precipitation, AMFs with hierarchical dendritic structure was successfully synthesized (Figs. 2a), the hierarchical structures can provide strong van der Waals forces. The resulting AMFs had a thickness ranging from 20 μm to 40 μm (Fig. 2a and Figs. S5 and S6 in ESI). XPS tests and XRD patterns revealed that the shear-induced precipitation of the prepared AMFs did not cause any structural damage (Fig. 2c and Fig. S8 in ESI). Fig. 1(b) shows the changes in molecular morphology that occur during the preparation of AMFs, while Fig. 1(c) provides a schematic representation of the structural changes in the molecular chains during the initial protonation process. Transmission electron microscopy (TEM) images displayed the binding of AMFs with LM particles, resembling the distribution of particles on a fiber network, akin to dry clay dispersed on tree roots (Fig. S11 in ESI). Fig. 1(d) depicts the interaction between LM and AMFs during the resetting process of the liquid metal interface. AMFs is not sensitive to solution environment. When pH=2 and 4, the surface of AMFs exhibits a negative charge (Fig. 2b). This is due to the fact that AMFs is obtained by deprotonation of PPTA yarn by strong alkaline KOH, which exhibits a negative charge. Despite partial protonation of AMFs in the IPA solution during the initial step, the protonation process remains incomplete, resulting in proton deletions within the AMFs structure, leading to the manifestation of negative charges. LM release Ga^{3+} ions through a spontaneous process of electron (e^-) transfer ($Ga - 3e^- = Ga^{3+}$).[34] Thus, the force between charges is always present between the process of interface reset. The surface interaction was further confirmed by the FTIR spectroscopy result. In the FTIR spectrum, the characteristic peak corresponding to the stretching vibration of N—H in AMFs can be observed at 3310 cm^{-1}. In the case of AMFs-pH/LM, a red-shift of approximately 30 cm^{-1} can be observed in this mode, indicating the presence of bonding interactions between LM and AMFs (Fig. 1e). As evidenced by the *in situ* IR spectra depicted in Fig. 1(f), the $\upsilon_{C=O}$ characteristic peaks of the aramid nanofibers solution remain unaltered upon the addition of IPA. This observation suggests a limited proton-donating capacity of IPA, which hinders the efficient restoration of the ANFs structure. However, with the subsequent introduction of water, the appearance of the $\upsilon_{C=O}$ characteristic peak indicates the successful restoration of the ANFs structure. As illustrated in Fig. S18 (in ESI), the UV intensity of the ANFs solution, following restoration by IPA, IPA pH=4, and H_2O reconfiguration, exhibits an enhancement compared to the UV absorption intensity when IPA or Water alone is added. This finding suggests that the reprotonation of ANFs is more favorable for the restoration of the ANFs structure.

Fig. 3(a) illustrates the granular presentation of LM following ultrasonic crushing. Fig. 3(b) shows that primary AMFs/70 wt% LM, LM granular distributing on the AMFs network, and Fig. 3(c) shows that LM interaction with AMFs becomes stronger after the LM interface is reset at pH=4 condition. The observation of enhanced adhesion between LM and AMFs signifies that the adjustment of pH levels contributes to the achievement of interfacial resetting. Fig. 3(d) showing the prepared AMFs has a hierarchical morphology. Hierarchical morphology leads to the storage modulus (G') and loss modulus (G'') of AMFs exhibit an increase of one order of magnitude compared to ANFs (Fig. S4 in ESI). Figs. 3(e) and 3(f) show that LM can be relative uniformly dispersed on AMFs. Fig. 3(g) and Fig. S13 (in ESI) provide cross-sectional analysis of the AMFs-pH/LM films, revealing their distinct laminated structures. Notably, these films are obtained subsequent to the process of reprotonation and interfacial reset. The examination of these cross-sectional images demonstrates a notable enhancement in film densification, accompanied by a significantly augmented interaction between the LM and

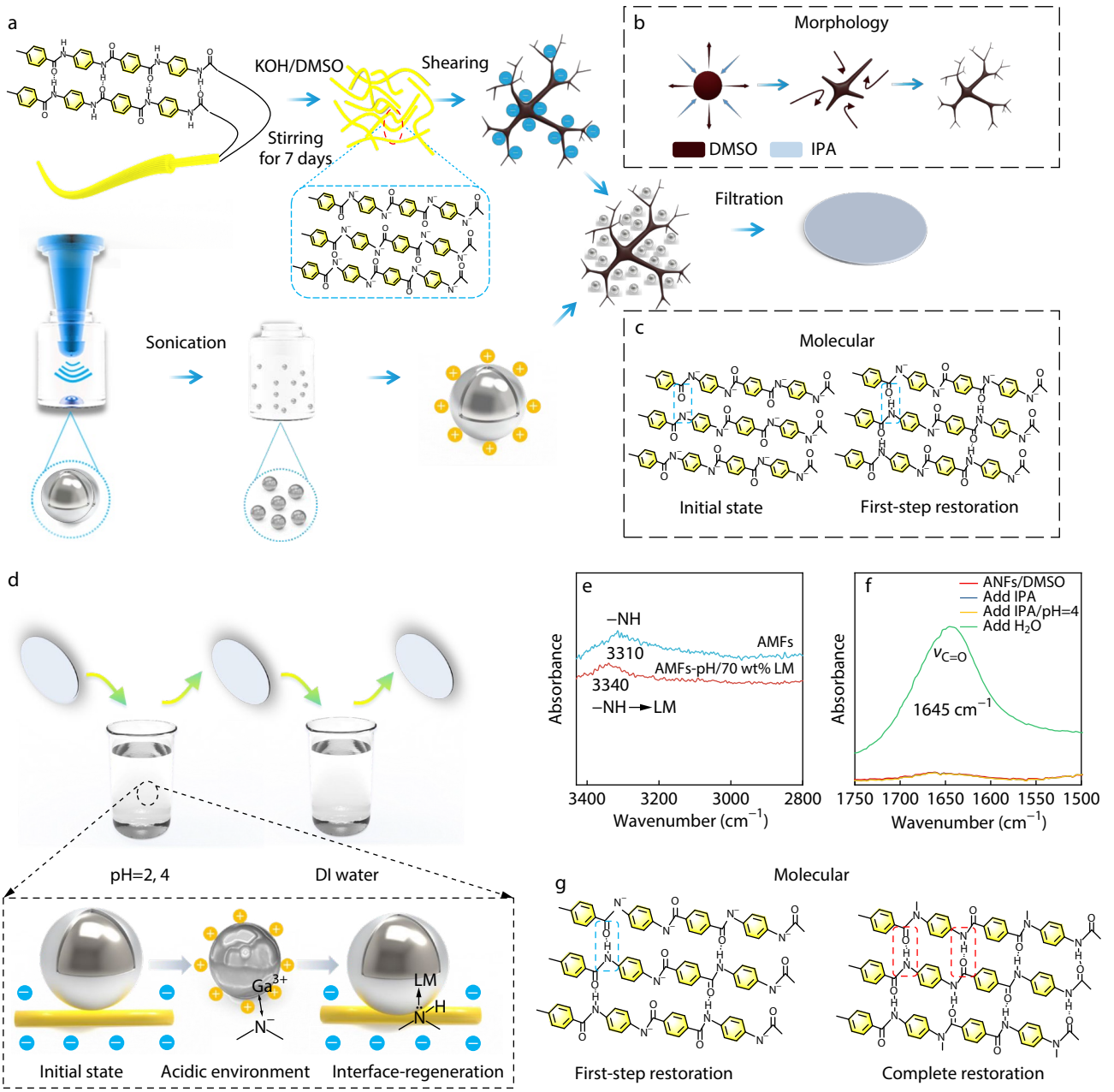

Fig. 1 (a) The schematic of the fabricating procedure of AMFs-pH/LM film; (b) Alterations in polymer morphology during processing techniques employing "Solvent exchange" methods; (c) Changes in polymer molecular during processing techniques employing "first-step protonation" methods; (d) LM interface reconfiguration and reprotonation of composite films; (e) Infrared spectra of bonding and interaction of LM with AMFs; (f) *In situ* infrared spectra of ANFs/DMSO; (g) Effect of multi-step protonation on AMFs chain structure.

AMFs constituents. EDS mapping images (Fig. 3g) further validate the homogeneity of LM distribution within the laminar composite film. As depicted in Fig. 1(f), the AMFs-pH/70wt% LM nanocomposite film exhibits remarkable mechanical resilience, as it can undergo repeated bending and folding without fracturing or sustaining noticeable damage. Moreover, this film showcases an exceptional load-bearing capability, as evidenced by the successful lifting of a substantial weight by a small-sized (5.0 mm × 30.0 mm, 46 mg) AMFs-pH/70 wt% LM paper. Notably, the paper effortlessly supports an object weighing 2 kg, surpassing an astonishing load-to-weight ratio of more than 232558 times its own mass. These findings unequivocally demonstrate exceptional load-bearing capacity and highlight its potential for robust and durable applications of the film.

As can be seen from Fig. 4, the suspension treated with shear-induced precipitation can be stably dispersed for several hours without fillers deposition. The suspension comprising AMFs and LM exhibits remarkable stability, remaining uniformly dispersed for extended durations without filler deposition. We postulate that this phenomenon can be attributed to hierarchical structure of AMFs acts as a robust tree roots, effectively capture LM,[35] coupled with the inherent stability exhibited by the AMFs/IPA colloid (Fig. S7 in ESI), preventing

https://doi.org/10.1007/s10118-024-3144-2

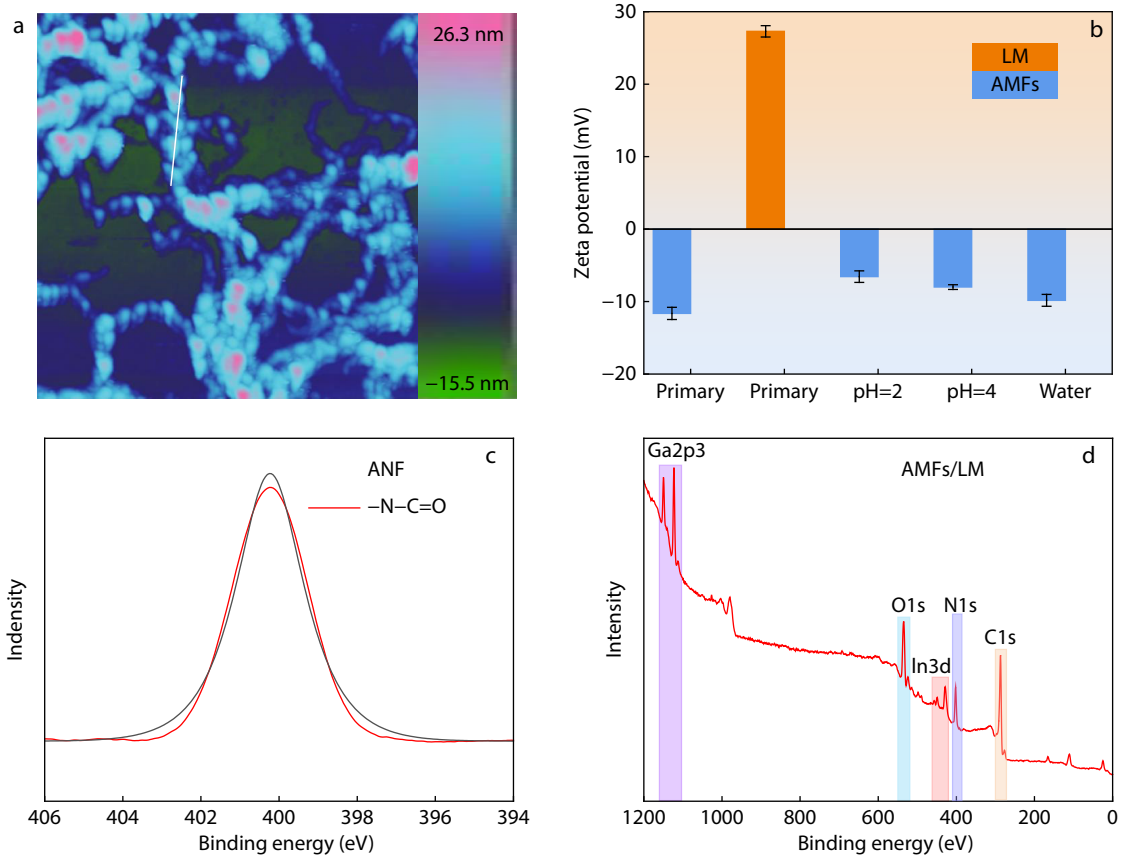

Fig. 2 (a) AFM images of AMFs; (b) Zeta potential of LM and AMFs under different acidic conditions; (c) XPS analysis of AMFs; (d) XPS analysis of AMFs/LM.

the settling or aggregation of the LM particles and ensuring their sustained suspension over time. Consequently, the harmonious dispersion of LM was achieved, owing to these factors.

The stress-strain curves and detailed mechanical properties of the films with various filler loadings are presented in Figs. 5(a)–5(e). The mechanical properties of the composite films, after undergoing reprotonation, surpass those of films protonated solely with IPA, owing to the restoration of the molecular chain structure of AMFs facilitated by reprotonation. This phenomenon can be attributed to the incomplete reconfiguration of AMFs after a weak proton supply from IPA. Solvent exchange and turbulent shear in IPA enable a gradual protonation process and the formation of AMFs. The formation of AMFs with fiber joints enhances the mechanical properties of the composites.[36] Furthermore, notable structural restoration is achieved through the utilization of deionized water (DI), a more potent proton donor solvent. This deliberate selection of a stronger proton donor solvent engenders a pronounced enhancement in the mechanical properties of the composite films. The ultimate strength of neat AMFs after reprotonation treatment could reach 178.21±1.62 MPa, which exceeds the ultimate strength of primary AMFs paper (153.53±2.52 MPa) by 16.1%. The microstructures of the fracture cross section of AMFs-pH/LM were shown by scanning electron microscopy images (Fig. S13 in ESI), upon altering the pH of the neat AMFs films, it is observed that the films continue to exhibit a layered structure. However, upon the introduction of LM, and as the LM content increases, a decline in the mechanical strength of the films becomes apparent. This decline can be attributed to the disruptive influence of the LM on the stacking arrangement of the AMFs network. Particularly, when pH=2, the film cross-section exhibits disorder, accompanied by an increase in the presence of defects. The rise in defect density further contributes to a significant decrease in the ultimate strength of the AMFs-pH/LM composites. On the other hand, the mechanical properties of the films treated with interfacial reset-reprotonation exhibit a notable improvement compared to those treated solely with water. Specifically, with the same filler content, the films subjected to interfacial reset-reprotonation experience an increase in ultimate strength by 17.0%, 5.4%, 24%, and 43.4% respectively, at filler contents of pH=4, 10%, 30%, 50%, and 70%, indicating that the interfacial reset-reprotonation treatment is beneficial to the mechanical properties of the films. Among them, it can be observed through (Fig. 3g) that the cross section of 70% AMFs-pH/LM is uniformly dispersed in the AMFs network and the stacking of the films is more dense after the interfacial reset at pH=4 and the reprotonation treatment of it. Particularly, at pH=2, the mechanical properties dramatically decrease with increasing LM content. This phenomenon can be attributed to the unfavorable impact of excessively acidic conditions during the LM interfacial reset process on the structure of composite film (Fig. S13 in ESI). How-

https://doi.org/10.1007/s10118-024-3144-2

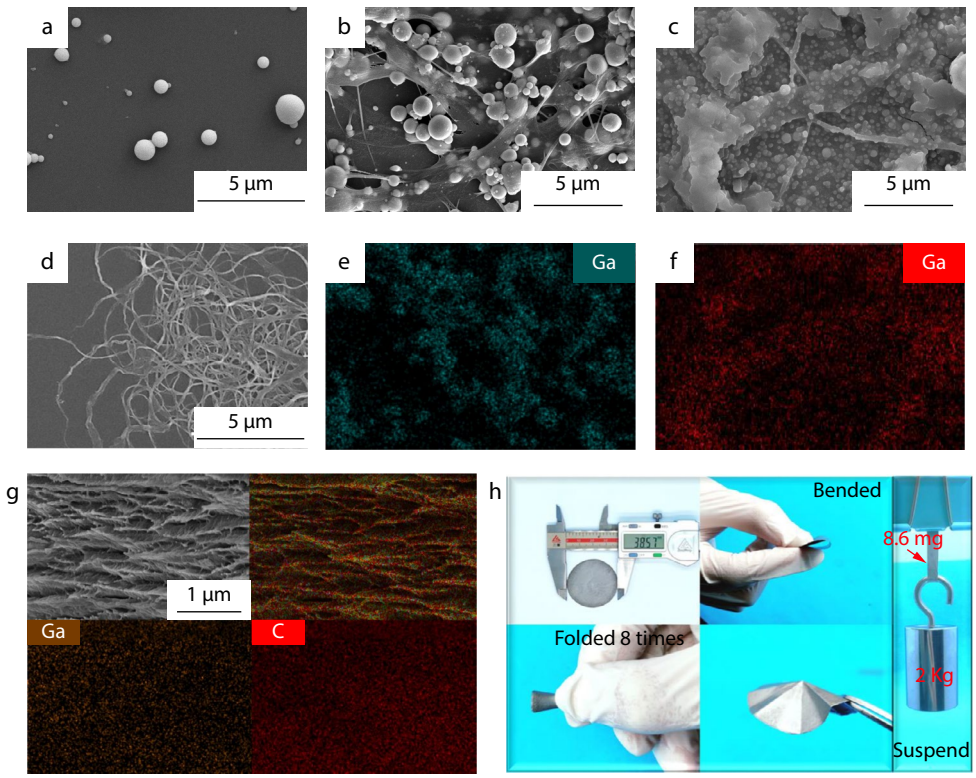

Fig. 3 (a) SEM image of LM after ultrasonic crushing; (b) Before LM perform interface reset; (c) After LM perform interface reset (pH=4); (d) Image of AMFs network showing hierarchical morphology; (e, f) SEM mapping images exhibit Ga element distribution; (g) SEM images and mapping of AMFs-pH/LM film and its tightly packed inner structure; (h) Optical photographs of AMFs-pH/70 wt% LM film showing the excellent flexibility.

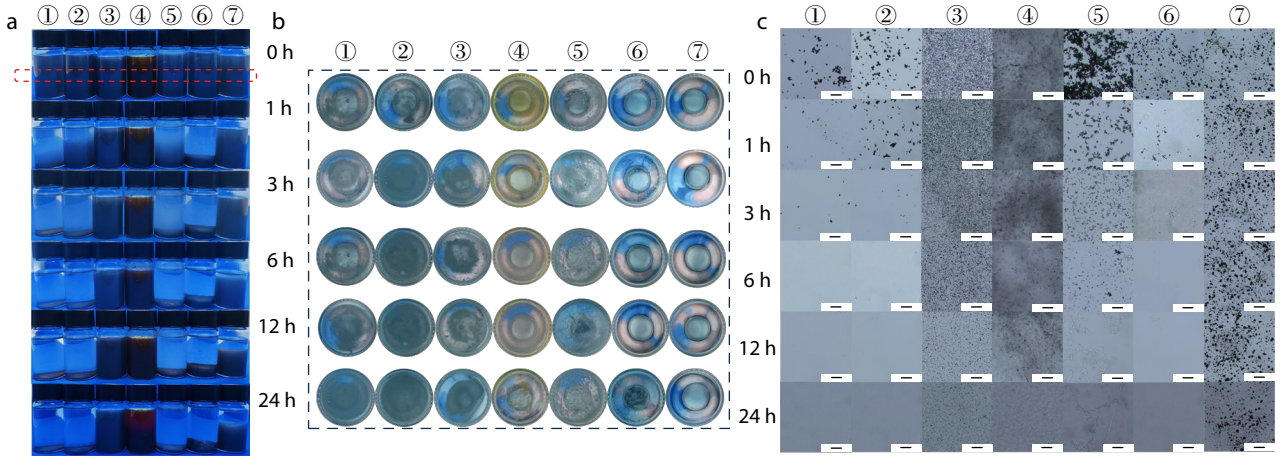

① LM dispersed in IPA ② LM dispersed in H_2O ③ LM dispersed in DMSO solution

④ LM dispersed in ANFs/DMSO solution without solvent exchange ⑤ LM dispersed in ANFs/water solution (conventional methods)

⑥ LM dispersed in ANFs without shear ⑦ LM dispersed in AMFs (shear-induced precipitation)

Fig. 4 Schematic diagram of AMFs assisted 70 wt% LM dispersion. (a) Front images were acquired at different time periods after the suspensions; (b) Bottom images were acquired at different moments after the suspensions only by gently turning it over; (c) OM (a.b.) images of middle of the solution at different moments after the suspensions. Scale bar=20 μm.

ever, at LM content of 70% and pH=4, the mechanical properties of the composite films maintain a favorable level. The tensile strength is measured at 85.88 MPa, and Young's modulus at 4.63 GPa, which are 1.76 and 1.36 times higher, respectively, than those of the single-step protonated films. Furthermore, we conducted further examinations of the mechanical properties of AMFs-pH/70 wt% LM films after subjecting them to 1000 tensile-refolding cycles (Fig. 5f, Fig. S19 in ESI). The mechanical properties slightly declined compared to the initial values but remained at the level of 70 MPa.

https://doi.org/10.1007/s10118-024-3144-2

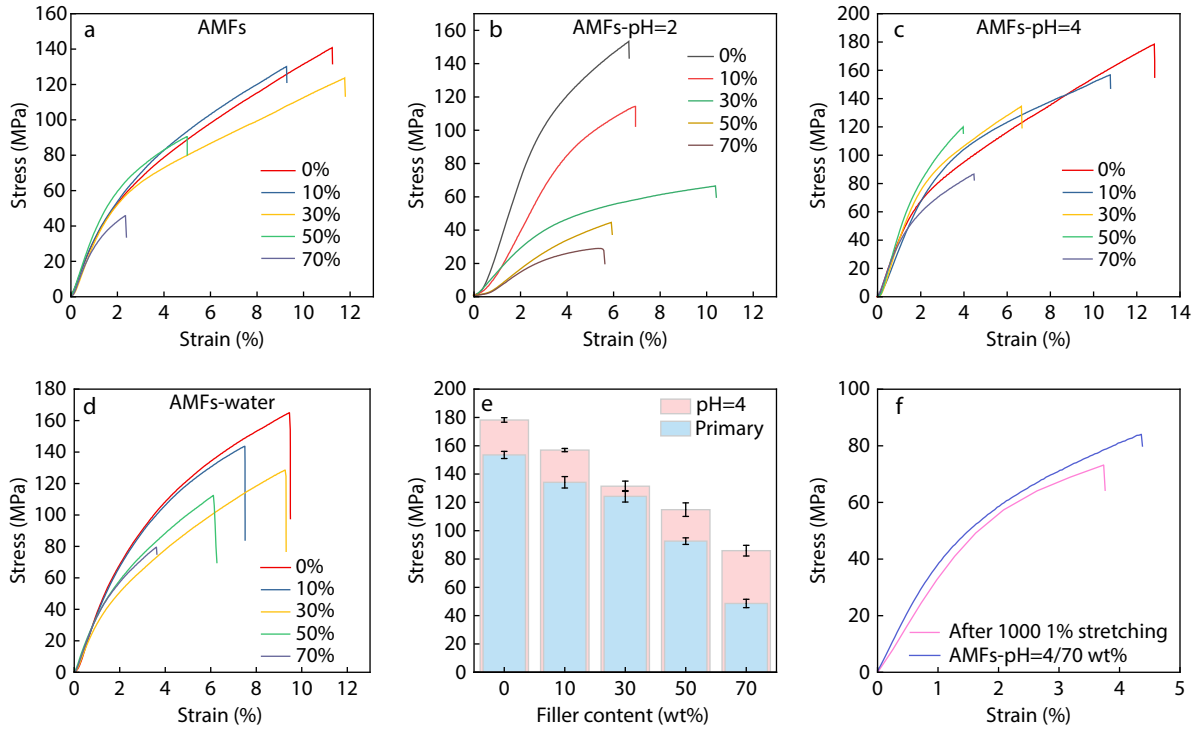

Fig. 5 (a–d) Typical stress-strain curves of AMFs/LM and AMFs-pH/LM films with different LM contents and different treatment conditions (AMFs-pH=2, 4, water); (e) Tensile strength enhancement after LM interface reset and protonation of AMFs; (f) Stress-strain curves of AMFs-pH=4/70 wt% LM film after 1000 stretch-fold cycles.

The thermal conductivities (TCs) of the films were quantified employing the laser flash method and subsequently graphed in Fig. 6(a), demonstrates the relationship between LM content and the thermal conductivity of ANFs/LM, AMFs/LM and AMFs-pH/LM composite films. Experimental results indicate the presence of anisotropic behavior in the thermal conductivity of the films, the TC of the AMFs-pH=4/70 wt% LM film is 10.98 $W \cdot m^{-1} \cdot K^{-1}$ at Fig. 6(e), improvement of 126.8% compared to ANFs/LM film, improvement of 58.2% compared to AMFs/LM film. The thermal conductivity enhancement efficiency (TCE%) of the AMFs-pH/LM obtained by this approach is more than 1500 times higher than that of films with 70% LM content. The improved thermal conductivity of the AMFs-pH/LM nanocomposite can be attributed to several factors. First, during vacuum-assisted filtration and the reprotonation process, the formation of a defect-reduced lamellar structure in the AMFs film enhances thermal conductivity.[51] Second, the AMFs aids in the construction of a local filler network, which establishes an efficient pathway for thermal transport and enhances the In-plane thermal conductivity. Third, the significant enhancement in the thermal conductivity of the AMFs-pH/LM nanocomposite can be attributed to improved interfacial compatibility between LM and the AMFs matrix. Through interfacial resetting, the force between LM and AMFs strengthens, allowing LM to effectively bridge the adjacent AMFs particles. This bridging facilitates the formation of thermally conductive channels for phonon transfer, minimizing phonon scattering at the filler-matrix interface, thereby reducing interfacial thermal resistance and enhancing thermal conductivity.[52,53] Fig. 6(d) and Fig. S22 (in ESI) show the composites prepared by this approach are superior to binary composite films containing only LM, and their thermal conductivity is close to that of some ternary composite films. It is worth mentioning that this method is also expected to be used in ternary systems, which provides a reference for the preparation of higher-performance composites containing liquid metal.

Considering the remarkable in-plane TC performance of the AMFs-pH/LM film, we investigated its impact on heat dissipation from a localized heat source by inserting the film between a 50 W high-power LED chip and an aluminum heat sink (Fig. 6b). Due to the much smaller thickness compared to its diameter of film, the contribution of out-of-plane TC to heat dissipation in the thickness direction can be considered negligible. Upon energizing the high-power LED, the surface temperature of the AMFs-pH/LM film increased from 25 °C to 121.3 °C within 60 s, showcasing a temperature reduction of 29.2 °C compared to the neat ANFs film, subsequently, the temperature gradually decreased to 31.5 °C within 240 s (Fig. 6f, Fig. S21 in ESI). Infrared images observation demonstrates the significant potential of AMFs-pH/LM films for effective thermal management of electronic devices subjected to high temperatures. Besides, Fig. 6(g) demonstrates that the films obtained using this method have better heat dissipation properties.

Significantly, the nanocomposite films demonstrated an exceptional level of electrical resistance (Fig. 6h). The remarkable resistivity observed in the AMFs-pH/LM films can be attributed to two primary factors, as we postulate. Firstly, despite the advantageous construction of a packing network facilitated by the dendritic polymer, there are limitations to achieving complete conductivity within the LM-based com-

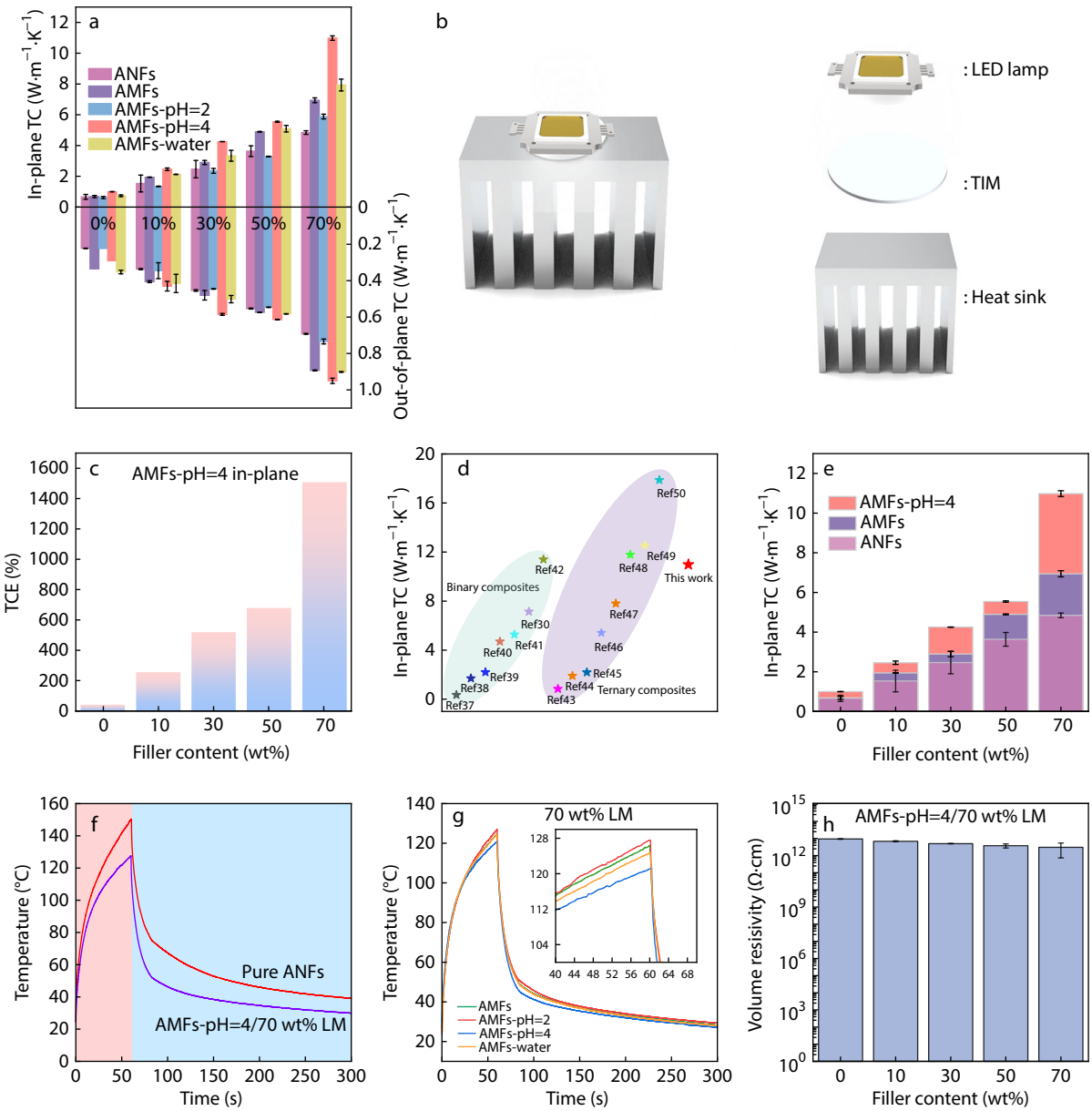

Fig. 6 (a) Thermal conductivity of different treatment conditions; (b) Schematic illustrating the measurement process for thermal interface materials; (c) The thermal conductivity improvement achieved by varying the filler content; (d) Comparison of thermal conductivity in the In-plane thermal conductivity with various reported LM composite material;[30,37–50] (e) Thermal conductivity enhancement after LM interface reset and protonation of AMFs; (f) The temperature-time relationship of the LED surface in the presence of ANFs and AMFs-pH=4/70 wt% LM as thermal interface materials; (g) The temperature-time relationship of the LED surface in the presence of different treatment conditions; (h) Volume resistivity of AMFs-pH=4/70 wt% LM composite and pure ANFs membranes.

posite films. While interfacial resetting enhances the interactions between LM and AMFs, the fusion between LM particles is not fully realized. The presence of an oxide layer on the LM surface further hampers the formation of a continuous conductive pathway. Consequently, the composite films exhibit elevated resistivity due to these factors impeding efficient electron flow. Secondly, the intricate hierarchical nanofiber network extensively covers the LM microspheres within the composite films. This augmented coverage significantly increases the contact resistance between the LM particles, hindering effective electron transfer across the film. As a result, the presence of the hierarchical nanofiber network contributes to the elevated resistivity observed in the LM-based composite films. Thus, the combination of incomplete fusion between LM particles and the obstructive effect of the hierarchical nanofiber network on LM microspheres contributes to the high resistivity exhibited by the LM-based composite films.

CONCLUSIONS

To conclude, we successfully prepared high-performance AMFs-pH/LM nanocomposite films using "shear-induced precipita-

tion-interfacial resetting-reprotonation" process. By combining van der Waals forces, electrostatic interactions, bonding of —NH to LM, as well as interfacial re-setting and multi-step protonation, we successfully enhance the interfacial interaction between LM and AMFs, increase its compatibility with the polymer, and achieve stable filler dispersion in the solvent. Furthermore, we achieve the construction of local filler network and the formation of filler-coated polymers, leading to an improved contribution of the filler to the polymer matrix. This approach enhances mechanical properties and thermal conductivity of the films. Compared to the AMFs/LM films, AMFs-pH=4/70 wt% LM exhibits significant mechanical properties, including tensile strength of ~85.88 MPa (77% increase), Young's modulus of ~4.63 GPa (36% increase), as well as significantly higher in-plane TC (10.98 $W{\cdot}m^{-1}{\cdot}K^{-1}$, an increase of % 126.8% compared to the ANFs/LM films). Meanwhile, the AMFs-pH/LM composite film has good thermal stability, flame retardancy, and electrical insulation (3.07×10^{12} Ω·cm).

Conflict of Interests

The authors declare no interest conflict.

Electronic Supplementary Information

Electronic supplementary information (ESI) is available free of charge in the online version of this article at http://doi.org/10.1007/s10118-024-3144-2.

Data Availability Statement

The data that support the findings of this study are available from the corresponding author upon reasonable request. The author's contact information: huadeng@scu.edu.cn.

ACKNOWLEDGMENTS

This work was financially supported by the National Key Research & Development Plan (No. 2022YFA1205200).

REFERENCES

1 Du, Y. K.; Shi, Z. X.; Dong, S.; Jin, H.; Ke, X.; Zhao, P.; Jiang, B. B.; You, F. Recent progress in fabrication and structural design of thermal conductive polymer composites. *Chinese J. Polym. Sci.* **2024**, *42*, 277–291.
2 Ji, Y.; Han, S. D.; Wu, H.; Guo, S. Y.; Zhang, F. S.; Qiu, J. H. Understanding the thermal impedance of silicone rubber/hexagonal boron nitride composites as thermal interface materials. *Chinese J. Polym. Sci*. **2023**, *42*, 352–363
3 Mani, D.; Vu, M. C.; Anand, S.; Kim, J. B.; Jeong, T. H.; Kim, I. H.; Seo, B. K.; Islam, M. A.; Kim, S. R. Elongated liquid metal based self-healing polyurethane composites for tunable thermal conductivity and electromagnetic interference shielding. *Compos. Commun.* **2023**, *44*, 101735.
4 Chen, Q.; Wang, Z. A copper organic phosphonate functionalizing boron nitride nanosheet for PVA film with excellent flame retardancy and improved thermal conductive property. *Compos. Part A: Appl. Sci. Manuf.* **2022**, *153*, 106738.
5 Chen, Q.; Ma, Z.; Wang, Z.; Liu, L.; Zhu, M.; Lei, W.; Song, P. Scalable, robust, low-cost, and highly thermally conductive anisotropic nanocomposite films for safe and efficient thermal management. *Adv. Funct. Mater.* **2022**, *32*, 2110782.
6 Tang, L.; Ruan, K.; Liu, X.; Tang, Y.; Zhang, Y.; Gu, J. Flexible and robust functionalized boron nitride/poly(*p*-phenylene benzobisoxazole) nanocomposite paper with high thermal conductivity and outstanding electrical insulation. *Nano-Micro Lett.* **2023**, *16*, 38.
7 Wang, S. S.; Feng, D. Y.; Zhang, Z. M.; Liu, X.; Ruan, K. P.; Guo, Y. Q.; Gu, J. W. Highly thermally conductive polydimethylsiloxane composites with controllable 3D GO@f-CNTs networks *via* self-sacrificing template method. *Chinese J. Polym. Sci*. **2024**, *42*, DOI: 10.1007/s10118-024-3098-4.
8 Kumar, S.; Singh, A.; Tiwari, M. Numerical and analytical modelling of effective thermal conductivity of multi-walled carbon nanotubes polymer nanocomposites including the effect of nanotube orientation and interfacial thermal resistance. *Nanocomposites* **2023**, *9*, 30–42.
9 Gao, M. Y.; Zhai, L.; Mo, S.; Jia, Y.; Liu, Y.; He, M. H.; Fan, L. Thermally conductive polyimide/boron nitride composite films with improved interfacial compatibility based on modified fillers by polyimide brushes. *Chinese J. Polym. Sci.* **2023**, *41*, 1921–1936.
10 Wang, X.; Liu, S.; Han, H.; Liu, X.; Wang, X. Research progress in insulating and thermal conductivity of fluorinated graphene and its polyimide composites. *IET Nanodielectrics* **2023**, DOI: 10.1049/nde2.12068.
11 Kwon, Y. J.; Park, J. B.; Jeon, Y. P.; Hong, J. Y.; Park, H. S.; Lee, J. U. A review of polymer composites based on carbon fillers for thermal management applications: design, preparation, and properties. *Polymers* **2021**, *13*, 1312.
12 Su, X.; Yang, Z.; Cheng, R.; Luvnish, A.; Han, S.; Meng, Q.; Stanford, N.; Ma, J. A comparative study of polycarbonate nanocomposites respectively containing graphene nanoplatelets, carbon nanotubes and carbon nanofibers. *Adv. Nanocompos.* **2024**, *1*, 77–85.
13 Xu, Y.; Xing, W.; Liu, J.; Song, C. Highly thermal conductive and rechargeable 3D liquid metal network-based phase change composite enabling photothermal pad. *Compos. Commun.* **2023**, *43*, 101719.
14 Guo, C.; He, L.; Yao, Y.; Lin, W.; Zhang, Y.; Zhang, Q.; Wu, K.; Fu, Q. Bifunctional liquid metals allow electrical insulating phase change materials to dual-mode thermal manage the Li-ion batteries. *Nano-Micro Lett.* **2022**, *14*, 202.
15 Guymon, G. G.; Malakooti, M. H. Multifunctional liquid metal polymer composites. *J. Polym. Sci.* **2022**, *60*, 1300–1327.
16 Guo, C.; Li, Y.; Xu, J.; Zhang, Q.; Wu, K.; Fu, Q. A thermally conductive interface material with tremendous and reversible surface adhesion promises durable cross-interface heat conduction. *Mater. Horiz.* **2022**, *9*, 1690–1699.
17 Chen, S.; Wang, H. Z.; Zhao, R. Q.; Rao, W.; Liu, J. Liquid metal composites. *Matter* **2020**, *2*, 1446–1480.
18 Bartlett, M. D.; Fassler, A.; Kazem, N.; Markvicka, E. J.; Mandal, P.; Majidi, C. Stretchable, high-*k* dielectric elastomers through liquid-metal inclusions. *Adv. Mater.* **2016**, *28*, 3726–3731.
19 Fassler, A.; Majidi, C. Liquid-phase metal inclusions for a conductive polymer composite. *Adv. Mater.* **2015**, *27*, 1928–1932.
20 Yan, J.; Malakooti, M. H.; Lu, Z.; Wang, Z.; Kazem, N.; Pan, C.; Bockstaller, M. R.; Majidi, C.; Matyjaszewski, K. Solution processable liquid metal nanodroplets by surface-initiated atom transfer radical polymerization. *Nat. Nanotechnol.* **2019**, *14*, 684–690.
21 Liao, M.; Liao, H.; Ye, J.; Wan, P.; Zhang, L. Polyvinyl alcohol-stabilized liquid metal hydrogel for wearable transient epidermal

sensors. *ACS Appl. Mater. Interfaces* **2019**, *11*, 47358–47364.
22 Chen, B.; Cao, Y.; Li, Q.; Yan, Z.; Liu, R.; Zhao, Y.; Zhang, X.; Wu, M.; Qin, Y.; Sun, C.; Yao, W.; Cao, Z.; Ajayan, P. M.; Chee, M. O. L.; Dong, P.; Li, Z.; Shen, J.; Ye, M. Liquid metal-tailored gluten network for protein-based e-skin. *Nat. Commun.* **2022**, *13*, 1206.
23 Ford, M. J.; Patel, D. K.; Pan, C.; Bergbreiter, S.; Majidi, C. Controlled assembly of liquid metal inclusions as a general approach for multifunctional composites. *Adv. Mater.* **2020**, *32*, 2002929.
24 Li, X.; Li, M.; Shou, Q.; Zhou, L.; Ge, A.; Pei, D.; Li, C. Liquid metal initiator of ring-opening polymerization: self-capsulation into thermal/photomoldable powder for multifunctional composites. *Adv. Mater.* **2020**, *32*, 2003553.
25 Chen, C.; Zhang, M.; Tian, K.; Fu, Q.; Deng, H. Dendritic structure-inspired coating strategy for stable and efficient solar evaporation of salinity brine. *ACS Sustainable Chem. Eng.* **2023**, *11*, 3882–3895.
26 Xia, L.; Zheng, X.; Yang, R.; Yuan, X.; Jiang, M.; Zhuang, X. Robust nanocomposite films with high dielectric insulation from boron nitride nanosheet and aramid nanofiber. *Fibers and Polymers* **2023**, *24*, 1131–1138.
27 Li, N.; Lu, Z.; Ji, X.; Ning, D.; E, S. Metal ion-assisted fabrication of aramid nanofilm with high strength and toughness for the dye separation. *Compos. Commun.* **2023**, *43*, 101702.
28 Huang, F. W.; Yang, Q. C.; Jia, L. C.; Yan, D. X.; Li, Z. M. Aramid nanofiber assisted preparation of self-standing liquid metal-based films for ultrahigh electromagnetic interference shielding. *Chem. Eng. J.* **2021**, *426*, 131288.
29 Zhou, G.; Yao, L.; Xie, Z.; Kamran, U.; Xie, J.; Zhang, F.; Park, S.-J.; Zhang, Y. Controllable construction of CNT-Interconnected liquid metal networks for thermal management. *Compos. Part A: Appl. Sci. Manuf.* **2023**, *175*, 107743.
30 Jia, L. C.; Jin, Y. F.; Ren, J. W.; Zhao, L. H.; Yan, D. X.; Li, Z. M. Highly thermally conductive liquid metal-based composites with superior thermostability for thermal management. *J. Mater. Chem. C* **2021**, *9*, 2904–2911.
31 Xie, J.; Zhou, G.; Sun, Y.; Zhang, F.; Kang, F.; Li, B.; Zhao, Y.; Zhang, Y.; Feng, W.; Zheng, Q. Multifunctional liquid metal-bridged graphite nanoplatelets/aramid nanofiber film for thermal management. *Small* **2024**, *20*, 2305163.
32 Roh, S.; Williams, A. H.; Bang, R. S.; Stoyanov, S. D.; Velev, O. D. Soft dendritic microparticles with unusual adhesion and structuring properties. *Nat. Mater.* **2019**, *18*, 1315–1320.
33 Yang, M.; Cao, K.; Sui, L.; Qi, Y.; Zhu, J.; Waas, A.; Arruda, E. M.; Kieffer, J.; Thouless, M. D.; Kotov, N. A. Dispersions of aramid nanofibers: a new nanoscale building block. *ACS Nano* **2011**, *5*, 6945–6954.
34 Wang, D.; Wang, X.; Rao, W. Precise regulation of Ga-based liquid metal oxidation. *Acc. Mater. Res.* **2021**, *2*, 1093–1103.
35 Zhao, G.; Cao, X.; Zhang, Q.; Deng, H.; Fu, Q. A novel interpenetrating segregated functional filler network structure for ultra-high electrical conductivity and efficient EMI shielding in CPCs containing carbon nanotubes. *Mater. Today Phys.* **2021**, *21*, 100483.
36 Xiong, L.; Wei, Y.; Chen, C.; Chen, X.; Fu, Q.; Deng, H. Thin lamellar films with enhanced mechanical properties for durable radiative cooling. *Nat. Commun.* **2023**, *14*, 6129.
37 Zhao, C.; Wang, Y.; Gao, L.; Xu, Y.; Fan, Z.; Liu, X.; Ni, Y.; Xuan, S.; Deng, H.; Gong, X. High-performance liquid metal/polyborosiloxane elastomer toward thermally conductive applications. *ACS Appl. Mater. Interfaces* **2022**, *14*, 21564–21576.
38 Ford, M. J.; Ambulo, C. P.; Kent, T. A.; Markvicka, E. J.; Pan, C.; Malen, J.; Ware, T. H.; Majidi, C. A multifunctional shape-morphing elastomer with liquid metal inclusions. *Proc. Natl. Acad. Sci. U. S. A.* **2019**, *116*, 21438–21444.
39 Jeong, S. H.; Chen, S.; Huo, J.; Gamstedt, E. K.; Liu, J.; Zhang, S. L.; Zhang, Z. B.; Hjort, K.; Wu, Z. Mechanically stretchable and electrically insulating thermal elastomer composite by liquid alloy droplet embedment. *Sci. Rep.* **2015**, *5*, 18257.
40 Bartlett, M. D.; Kazem, N.; Powell-Palm, M. J.; Huang, X.; Sun, W.; Malen, J. A.; Majidi, C. High thermal conductivity in soft elastomers with elongated liquid metal inclusions. *Proc. Natl. Acad. Sci. U. S. A.* **2017**, *114*, 2143–2148.
41 Yu, D.; Liao, Y.; Song, Y.; Wang, S.; Wan, H.; Zeng, Y.; Yin, T.; Yang, W.; He, Z. A Super-stretchable liquid metal foamed elastomer for tunable control of electromagnetic waves and thermal transport. *Adv. Sci.* **2020**, *7*, 2000177.
42 Haque, A. B. M. T.; Tutika, R.; Byrum, R. L.; Bartlett, M. D. Programmable liquid metal microstructures for multifunctional soft thermal composites. *Adv. Funct. Mater.* **2020**, *30*, 2000832.
43 Sargolzaeiaval, Y.; Ramesh, V. P.; Neumann, T. V.; Miles, R.; Dickey, M. D.; Öztürk, M. C. High thermal conductivity silicone elastomer doped with graphene nanoplatelets and eutectic GaIn liquid metal alloy. *ECS J. Solid State Sci. Technol.* **2019**, *8*, 357.
44 Xie, Z.; Xue, R.; Dou, Z.; Xiao, L.; Li, Y.; Zhang, Q.; Fu, Q. Largely enhanced dielectric and thermal conductive properties of polypropylene composites by adding mixture of exfoliated boron nitride and liquid metal. *Compos. Part A: Appl. Sci. Manuf.* **2022**, *161*, 107081.
45 Yi, S. Q.; Sun, H.; Jin, Y. F.; Zou, K. K.; Li, J.; Jia, L. C.; Yan, D. X.; Li, Z. M. CNT-assisted design of stable liquid metal droplets for flexible multifunctional composites. *Compos. Part B: Eng.* **2022**, *239*, 109961.
46 Luo, F.; Cui, W.; Zou, Y.; Li, H.; Qian, Q. Thermal conductivity and closed-loop recycling of bulk biphenyl epoxy composites with directional controllable thermal pathways. *J. Mater. Chem. A* **2023**, *11*, 15456–15465.
47 Ran, L.; Ma, X.; Qiu, L.; Sun, F.; Zhao, L.; Yi, L.; Ji, X. Liquid metal assisted fabrication of MXene-based films: Toward superior electromagnetic interference shielding and thermal management. *J. Colloid Interface Sci.* **2023**, *652*, 705–717.
48 Zhang, C.; Wang, M.; Lin, X.; Tao, S.; Wang, X.; Chen, Y.; Liu, H.; Wang, Y.; Qi, H. Holocellulose nanofibrils assisted exfoliation of boron nitride nanosheets for thermal management nanocomposite films. *Carbohydr. Polym.* **2022**, *291*, 119578.
49 Lv, Z.; Kong, L.; Sun, P.; Lin, Y.; Wang, Y.; Xiao, C.; Liu, X.; Zhang, X.; Zheng, K.; Tian, X. Dual-functional eco-friendly liquid metal/boron nitride/silk fibroin composite film with outstanding thermal conductivity and electromagnetic shielding efficiency. *Compos. Commun.* **2023**, *39*, 101565.
50 Chen, S.; Xing, W.; Wang, H.; Cheng, W.; Lei, Z.; Zheng, F.; Tao, P.; Shang, W.; Fu, B.; Song, C.; Dickey, M. D.; Deng, T. A bottom-up approach to generate isotropic liquid metal network in polymer-enabled 3D thermal management. *Chem. Eng. J.* **2022**, *439*, 135674.
51 Chen, Q.; Ma, Z.; Wang, M.; Wang, Z.; Feng, J.; Chevali, V.; Song, P. Recent advances in nacre-inspired anisotropic thermally conductive polymeric nanocomposites. *Nano Res.* **2023**, *16*, 1362–1386.
52 Chen, Q.; Huo, S.; Lu, Y.; Ding, M.; Feng, J.; Huang, G.; Xu, H.; Sun, Z.; Wang, Z.; Song, P. Heterostructured graphene@silica@iron phenylphosphinate for fire-retardant, strong, thermally conductive yet electrically insulated epoxy nanocomposites. *Small* **2024**, DOI: 10.1002/smll.202310724.
53 Chen, Q.; Liu, L.; Zhang, A.; Wang, W.; Wang, Z.; Zhang, J.; Feng, J.; Huo, S.; Zeng, X.; Song, P. An iron phenylphosphinate@graphene oxide nanohybrid enabled flame-retardant, mechanically reinforced, and thermally conductive epoxy nanocomposites. *Chem. Eng. J.* **2023**, *454*, 140424.

https://doi.org/10.1007/s10118-024-3144-2